THE JOURNAL OF BIOLOGICAL CHEMISTRY VOL. 291, NO. 31, pp. 16292–16306, July 29, 2016

Crystal Structures of the Human Doublecortin C- and N-terminal Domains in Complex with Specific Antibodies*

Received for publication, March 11, 2016, and in revised form, May 3, 2016 Published, JBC Papers in Press, May 10, 2016, DOI 10.1074/jbc.M116.726547

Dominique Burger[‡], Martine Stihle[‡], Ashwani Sharma[§], Paola Di Lello[¶1], Jörg Benz[‡], Brigitte D'Arcy[‡], Maja Debulpaep[‖], David Fry[¶], Walter Huber[‡], Thomas Kremer[‡‡], Toon Laeremans[‖**], Hugues Matile[‡], Alfred Ross[‡], Arne C. Rufer[‡], Guillaume Schoch[‡‡2], Michel O. Steinmetz[§], Jan Steyaert[‖**], Markus G. Rudolph[‡], Ralf Thoma[‡], and Armin Ruf[‡3]**

*From the [‡]pRED Pharma Research and Early Development, Therapeutic Modalities, and [‡‡]Roche Pharmaceutical Research and Early Development, NORD Discovery and Translational Area, Roche Innovation Center Basel, F. Hoffmann-La Roche Ltd., Grenzacherstrasse 124, 4070 Basel, Switzerland, the [§]Laboratory of Biomolecular Research, Department of Biology and Chemistry, Paul Scherrer Institut, 5232 Villigen PSI, Switzerland, [¶]pRED Pharma Research and Early Development, Small Molecule Research, Discovery Technologies, Roche, Nutley, New Jersey 07110, [‖]Structural Biology Brussels, Vrije Universiteit Brussel, Pleinlaan 2, 1050 Brussels, Belgium, and the **Structural Biology Research Center, VIB, Pleinlaan 2, 1050 Brussels, Belgium*

Doublecortin is a microtubule-associated protein produced during neurogenesis. The protein stabilizes microtubules and stimulates their polymerization, which allows migration of immature neurons to their designated location in the brain. Mutations in the gene that impair doublecortin function and cause severe brain formation disorders are located on a tandem repeat of two doublecortin domains. The molecular mechanism of action of doublecortin is only incompletely understood. Anti-doublecortin antibodies, such as the rabbit polyclonal Abcam 18732, are widely used as neurogenesis markers. Here, we report the generation and characterization of antibodies that bind to single doublecortin domains. The antibodies were used as tools to obtain structures of both domains. Four independent crystal structures of the N-terminal domain reveal several distinct open and closed conformations of the peptide linking N- and C-terminal domains, which can be related to doublecortin function. An NMR assignment and a crystal structure in complex with a camelid antibody fragment show that the doublecortin C-terminal domain adopts the same well defined ubiquitin-like fold as the N-terminal domain, despite its reported aggregation and molten globule-like properties. The antibodies' unique domain specificity also renders them ideal research tools to better understand the role of individual domains in doublecortin function. A single chain camelid antibody fragment specific for the C-terminal doublecortin domain affected microtubule binding, whereas a monoclonal mouse antibody specific for the N-terminal domain did not. Together with steric considerations, this suggests that the microtubule-interacting doublecortin domain observed in cryo-electron micrographs is the C-terminal domain rather than the N-terminal one.

Doublecortin is a microtubule-associated protein that is essential for normal human brain development. Missense mutations in the doublecortin gene cause defective cortical neuronal migration, leading to the brain formation disorders X-linked lissencephaly and subcortical band heterotopia (1). Doublecortin-deficient neurons also show defects in the kinesin-3-motor protein-mediated transport of presynaptic vesicles (2). Anti-doublecortin antibodies are widely used as markers in the immunohistochemical detection of neurogenesis (3) and are therefore important research tools for neuroscience. Recently, basal doublecortin levels were also reported outside of neurogenic regions in the brain (4). From two clusters of mutations in X-linked lissencephaly and subcortical band heterotopia patients, an internal tandem repeat of domains with 27% sequence identity was identified on the doublecortin gene, *DCX*. These domains were also detected in sequences of other proteins and are called DCX domains. In doublecortin, a serine/proline-rich tail is located C-terminal of this DCX domain tandem repeat. The patient mutations lead to impaired tubulin polymerization both *in vitro* and *in vivo* as well as impaired microtubule stabilization (5). Although individual patient mutations occur in both DCX domains with similar frequencies, recurrent mutations increase the overall number in the C-terminal domain (6). The DCX domain tandem repeat significantly enhances microtubule polymerization, whereas individual DCX domains alone do not (5, 7).

In vitro no single DCX domain is sufficient for co-assembly with taxol-induced microtubules, and only doublecortin constructs encompassing at least the DCX domain tandem repeat co-assemble with microtubules, even when produced in *Escherichia coli*, suggesting that post-translational modification of DCX is not required (5). However, NMR ^{1}H-^{15}N

* This work was supported by an EMBO Long Term Fellowship (to A. S.) as well as Swiss National Science Foundation Grant 310030B_138659 (to M. O. S.). The authors declare that they have no conflicts of interest with the contents of this article.

The atomic coordinates and structure factors (codes 5IN7, 5IO9, 5IOI, 5IKC, and 5IP4) have been deposited in the Protein Data Bank (http://wwpdb.org/).

The chemical shift assignment for C-DCX has been deposited in the BioMagnResBank (www.bmrb.wisc.edu) under accession number 26727.

[1] Present address: Dept. of Structural Biology, Genentech, 1 DNA Way, South San Francisco, CA 94080.

[2] Present address: Fishawack Archimed AG, Elisabethenanlage 11, 4051 Basel, Switzerland.

[3] To whom correspondence should be addressed: pRED Pharma Research and Early Development, Therapeutic Modalities, Chemical Biology, F. Hoffmann-La Roche Ltd., CH4070 Basel, Switzerland. Tel.: 41-61-6887750; E-mail: armin.ruf@roche.com.

HSQC[4] spectra on the isolated N- and C-terminal DCX domains showed line broadening in the presence of microtubules consistent with binding of individual domains to microtubules (7). Also, cryo-electron microscopy of doublecortin-stabilized microtubules visualizes only a single DCX domain bound, which was hypothesized to be N-DCX (8–10). The effect of patient mutations in fluorescence microscopy binding assays indicated that both DCX domains are involved in cooperative binding of doublecortin to 13-protofilament microtubules (11, 12). Similar experiments showed that single DCX molecules recognize the ends of growing microtubules by their concave lattice curvature and that only patient mutations on C-DCX abolish this (12). These mutations on C-DCX map to the contact sites between the DCX domain and microtubules observed in the cryo-EM reconstructions, suggesting that the bound DCX domain could be C-DCX instead of N-DCX (8, 12).

Two structures of the human doublecortin N-DCX domain were determined previously by NMR spectroscopy and by x-ray crystallography and display a fold with distinct similarity to members of the ubiquitin-like superfamily (7, 13). The crystal structure of the K215D/K216D mutant of the N-DCX domain ($N\text{-}DCX_{DD}$) had its C-terminal residues 220–228 in an extended "open" conformation, whereas the NMR structure of the wild type N-DCX indicated that residues 220–228 assume predominantly a "closed" helical conformation, similar to the conformation found in the crystal structure of the corresponding domain from doublecortin-like kinase, where the side chain of Trp^{150} (Trp^{227} in DCX) stacks against an Arg on the domain core. It was proposed that the switching between the open and closed conformations is of functional importance in the control of tubulin polymerization and microtubule bundling by doublecortin, although the observed open conformation was stabilized by crystal packing interactions (13). In contrast to N-DCX, the structure of C-DCX could previously be solved neither by crystallography nor by NMR methods. C-DCX showed no temperature or guanidine HCl-induced cooperative unfolding and exposed hydrophobic surface areas that bind the dye 8-anilino-1-naphtalene sulfonate (ANS). Furthermore, the NMR spectra of C-DCX could only be obtained at low protein concentrations and showed line broadening. Gel filtration of C-CDX showed a predominant monomeric fraction in equilibrium with oligomers, and the extensive Stokes radius calculated from the elution volume indicated a molten globule (7). The C-terminal domain of doublecortin domain-containing protein 2 (DCDC2) has 32% sequence identity with C-DCX and has a DCX fold according to its NMR structure with the PDB code 2DNF.

The objective of the present study was to obtain a deeper understanding of the structure and function of individual DCX domains of doublecortin. Because antibodies against DCX domains were not available, we generated antibodies specific to single DCX domains of doublecortin. We assessed whether these antibodies modulate the microtubule interaction of T-DCX *in vitro*. We used them as crystallization helpers to obtain the first high resolution structures of a C-DCX domain and of wild type human N-DCX. Assignment of the two-dimensional $^{1}H\text{-}^{15}N$ HSQC NMR peaks further showed that C-DCX is folded in solution in the absence of an antibody. We also obtained several independent structures of N-DCX. Among these are the first observations of distinct closed conformations of N-DCX in a crystal and a new open conformation. Together they describe in detail the flexibility of the linker region positioned C-terminally of the N-DCX core domain, which is important for doublecortin function. Taken together, our results suggest that C-DCX is the doublecortin domain observed interacting with microtubules in cryo-EM studies.

Experimental Procedures

Construct Design of Doublecortin Variants—For consistency with databases, we use the UNIPROT human doublecortin numbering, which is shifted by 81 compared with the numbering used in previous reports on structures and patient mutations (Fig. 1*e*). A GeneArt *Escherichia coli*-optimized synthetic gene of human doublecortin was ordered from Qiagen (Hs_DCX_1_EC QIAgenes Expression Kit *E. coli* (EEC0013818)). Variants differing in length were amplified with iProof (Bio-Rad) and cloned into the pCR2.1 (Blunt Topo)-vector (Invitrogen). These constructs comprise single or both human doublecortin domains and include full-length human doublecortin (hDCX, Met^{82}–Met^{441}), the doublecortin tandem domains (T-DCX, Ala^{126}–Lys^{356}), the N-terminal doublecortin domain (N-DCX; the two variants Ala^{126}–Val^{231} and Ala^{133}–Val^{231}), and the C-terminal doublecortin domain (C-DCX; the two variants Ala^{251}–Ala^{341} and Lys^{255}–Lys^{356}). For the obtained clones, the inserts were checked by sequencing, cut out with NdeI/NotI, and cloned into pER7 and pER2b by ligation with T4 ligase (New England Biolabs). pER7 and pER2b are based on pET28 a(+) (Stratagene) and are constructed by inserting between the NcoI and NdeI restriction sites a sequence coding for a His_6 tag fused to GST or a sequence coding for a His_6 tag fused to SUMO, both followed by a thrombin cleavage site, respectively. The $N\text{-}DCX_{DD}$ double mutation K215D/K216D that reduced the calculated pI and the number of high entropy N-DCX surface side chains, thus improving its crystallization properties (13), was introduced to both N-DCX variants by using the QuikChange multisite-directed mutagenesis kit from Stratagene (La Jolla, CA).

Production and Purification of Doublecortin Variants—For production of His_6-GST-hDCX or His_6-SUMO-hDCX fusion proteins at an analytical scale, transformed *E. coli* BL21(DE3) cells were grown at 37 °C in 3 ml of LB medium supplemented with 75 μg/ml of kanamycin for maintenance of vector. After an A_{600} of 0.4–0.5 was reached, cells were incubated for 30 min at

[4] The abbreviations used are: HSQC, heteronuclear single quantum correlation; ANS, 8-anilino-1-naphtalene sulfonate; C-DCX, C-terminal doublecortin domain of human doublecortin; CDR, complementarity-determining region in immunoglobulin variable chain; Fab, antigen-binding fragment of antibody; hDCX, human doublecortin residues 82–441; N-DCX, N-terminal doublecortin domain of human doublecortin; SPR, surface plasmon resonance; AUC, analytical ultracentrifugation; T-DCX, protein including the doublecortin domain tandem of human doublecortin; V_{HH}, variable domain of a heavy chain-only camelid antibody; SUMO, small ubiquitin-like modifier; TCEP, tris(2-carboxyethyl)phosphine; SEC, size exclusion chromatography; PDB, Protein Data Bank; r.m.s., root mean square; BisTris, 2-[bis(2-hydroxyethyl)amino]-2-(hydroxymethyl)propane-1,3-diol.

20 °C, followed by the addition of 0.5 mM isopropyl 1-thio-β-D-galactopyranoside to induce expression, and further grown overnight at 20 °C.

Because the DCX variants with the SUMO tag were expressed and purified much better, mainly these were used for large scale purification. 50 g of cells were resuspended in 200 ml of 50 mM HEPES, 300 mM NaCl, 2 mM $MgCl_2$, 5 mM diisopropyl fluorophosphate (catalog no. 38399; Fluka), 2 mM TCEP, pH 7.5, supplemented with DNase I (Roche Applied Science) (1 mg/50 ml) and an EDTA-free protease inhibitor mixture (Roche Applied Science) (1 tablet/50 ml). The cell suspension was lysed with cell disruption equipment BasicZ with 0.8 kilobar pressure (Constant System) and centrifuged (Sorvall/RC5B, SS34, 45 min, 32,000 × *g*, 4 °C) to separate the soluble from the insoluble fraction of the cell extract. The 0.22-μm filtered soluble supernatant was loaded onto a nickel-Sepharose column (HisTrap HP 5 ml; catalog no. 17-5247-01, GE Healthcare), and equilibrated with 50 mM Hepes, 300 mM NaCl, 2 mM TCEP, pH 7.5. The column was washed with the equilibration buffer, and the bound His_6-tagged protein was eluted by applying a linear gradient of 0–300 mM imidazole. Fractions containing the His_6-SUMO-hDCX fusion protein were pooled and supplemented with SUMO-protease (catalog no. 12588-018, Invitrogen) or alternatively supplemented with thrombin (catalog no. 27-0846-01, GE Healthcare) and 2.5 mM $CaCl_2$ final concentration in the buffer. The sample was dialyzed extensively with a Slide-a.Lyzer (molecular weight cut-off 3500) at 4 °C against 50 mM Hepes, pH 7.5, 100 mM NaCl, 10% glycerin, 8 mM CHAPS, 2 mM TCEP. For separation of the cleaved His_6-SUMO from the target protein, the sample was loaded onto a nickel-Sepharose column (HisTrap FF crude 1 ml, GE Healthcare), and equilibrated with 50 mM Hepes, 300 mM NaCl, 2 mM TCEP, pH 7.5. Samples cleaved with SUMO protease therefore contain additionally the N-terminal reminder of the thrombin cleavage site (*e.g.* ^{125}LVPRGSHM^{132} in N-DCX Ala^{133}–Val^{231}).

To remove remaining impurities, the flow-through was loaded onto a size exclusion column (S75 10/300 GL (catalog no. 17-5174-01), GE Healthcare), and equilibrated with 20 mM CAPS, pH 10.5; 100 mM NaCl; 5 mM TCEP or 20 mM Hepes, pH 7.5; 100 mM NaCl; 5 mM DTT or 20 mM sodium acetate, pH 4.0, 100 mM NaCl; 5 mM β-mercaptethanol. The fractions containing doublecortin variant were pooled and analyzed by SDS-PAGE, which showed that the proteins were at least 95% pure.

Thermofluor Buffer Screen—A fluorescence-based thermal shift assay was applied to identify optimal buffer compositions for structural studies as proposed by Ericsson *et al.* (14, 15). 1 μM C-DCX 252–356 was preincubated with the fluorescence probe Sypro Orange (Molecular Probes) in different buffer conditions. The fluorescence signal was recorded on a Bio-Rad MyiQ real-time PCR machine with an excitation wavelength of 490 nm and an emission wavelength of 530 nm (the absorption and emission maxima of Sypro Orange are 470 and 570 nm, respectively) and a heating rate of 1 °C/min. Measured fluorescence intensity values of protein melting transitions were normalized, fitted to a Boltzmann sigmoidal equation to calculate *Tm*, and plotted between 40 and 80 °C (GraphPad Prism).

Raising Mouse Monoclonal Antibodies against hDCX and Production of Fab1/108—For generation of novel anti-hDCX mAbs, Naval Medical Research Institute mice were immunized intraperitoneally with hDCX 82–441. The serum was tested for the presence of anti-hDCX antibodies by ELISA. Animals with strong immune response were selected for fusion, and the mAbs were prepared using a protocol described previously (16). Antibody mAb 1/108 was sequenced under contract by GenScript. It is of the IgG2b class, and the sequences of heavy and light chains are MKFSWVIFFLMAVVTGVNSEVQLQQSGADLVRPGASVKLSCTASGFDIKDDYVHWVKQRPEQGLEWIGRIDPANGATKYAPKFQDKATLTADTSSNTAYLQLSSLTSEDTAVYYCGRSKYFDSWGQGTTLTVSSAKTTPPSVYPLAPGCGDTTGSSVTLGCLVKGYFPESVTVTWNSGSLSSSVHTFPALLQSGLYTMSSSVTVPSSTWPSQTVTCSVAHPASSTTVDKKLEPSGPISTINPCPPCKECHKCPAPNLEGGPSVFIFPPNIKDVLMISLTPKVTCVVVDVSEDDPDVQISWFVNNVEVHTAQTQTHREDYNSTIRVVSTLPIQHQDWMSGKEFKCKVNNKDLPSPIERTISKIKGLVRAPQVYILPPPAEQLSRKDVSLTCLVVGFNPGDISVEWTSNGHTEENYKDTAPVLDSDGSYFIYSKLNMKTSKWEKTDSFSCNVRHEGLKNYYLKKTISRSPGK and MEFQTQVFVFVLLWLSGVDGDIVMTQSQKLMSTSVGDRVSITCKASQIVDTAVAWYQQKPGQSPKPLIYLASNRHTGVPDRFTGSGSGTDFTLTINNVQSDDLADYFCLQHWNYPLTFGAGTKLELKGADAAPTVSIFPPSSEQLTSGGASVVCFLNNFYPKDINVKWKIDGSERQNGVLNSWTDQDSKDSTYSMSSTLTLTKDEYERHNSYTCEATHKTSTSPIVKSFNRNEC, respectively.

To produce Fab1/108 for crystallization, mAb 1/108 was cleaved with papain at 293 K for 1 day, the reaction was stopped using the cysteine protease inhibitor E64, and the antibody Fab was separated from Fc and remaining mAb by sequential chromatography on a protein A column with a final polishing step by size exclusion chromatography (SEC). The T-DCX·Fab complexes were formed by mixing T-DCX and Fab in a molar ratio of 1:1.5. The complexes were purified by SEC (TSK G3000SW), and the complex-containing fractions were selected by simultaneous multiangle light-scattering analysis (TriStar, Wyatt Technology).

Raising and Producing Llama V_{HH} against C-DCX—Antibody Fab fragments are established as crystallization helpers (17, 18). The corresponding fragments of camelid heavy chain-only antibodies (V_{HH} or Nanobodies™) have only one "Ig domain" (19, 20). Such V_{HH} are often called "Xaperones™" when used for crystallization and have been applied to conformationally stabilize unstructured protein domains, transmembrane proteins, and protein complexes for crystallization (21). C-DCX-specific Xaperones were generated by a protocol similar to that described previously (22). Two llamas were immunized four times with T-DCX. Four and 8 days after the final antigen boost, peripheral blood lymphocytes were extracted, and their RNA was purified and converted into cDNA via RT-PCR. The Xaperone repertoire was cloned into a phage display/expression vector (pMESy4), containing a C-terminal His_6 and EPEA tag, resulting in two Xaperone libraries. In parallel biopanning experiments, the target protein was solid phase immobilized or captured via an antibody or neutravidin. Xaperones that bind T-DCX and also C-DCX were identified.

For characterization, the His-tagged Xaperones were produced periplasmically in *E. coli* WK6 cultures on a 24-well plate and purified by nickel-nitrilotriacetic acid superflow. C-DCX was mixed with a 1.5-fold excess of Xaperones followed by a 1-h incubation at room temperature. The complex was separated from the unbound Xaperone by SEC (S75 column), and the stoichiometries of the complexes were determined by RP-HPLC. For subsequent large scale preparation, selected Xaperones were purified directly from the periplasmic extract on a HisTrap column followed by SEC. The sequence of C-DCX-specific XA4551 was determined to be QVQLQESGGGLVQAGGSLRLSCTASVNIIGGNHWAWYRQAPGQQRDLVASLSRYNANYADSVKGRFTISRDNAKNAAYLQMNSLKPEDTAIYFCALENYYWGQGTQVTVSSHHHHHHHEPEA.

Microtubule Binding Experiments—Taxol-stabilized microtubules were used in a standard microtubule pelleting assay to test the binding of various protein samples with microtubules (23). For preparing taxol-microtubules, 10 μM tubulin in BRB-80 buffer (80 mM PIPES-KOH, pH 6.8, 1 mM $MgCl_2$, 1 mM EGTA) supplemented with 0.5 mM GTP was incubated at 37 °C for 10 min. 1/100 volume of 20 μM, 200 μM, and 2 mM taxol was added in a stepwise manner with a 5-min incubation time at 37 °C in between. Various test proteins plus taxol-microtubules and controls were incubated at room temperature for 15 min (reaction mix). A taxol-glycerol cushion (BRB-80 buffer supplemented with 40% glycerol and 20 μM taxol) was also incubated at room temperature for 15 min. Microtubule binders (pellet fraction) were separated from non-binders (supernatant fraction) by centrifugation on a taxol-glycerol cushion at 70,000 rpm for 30 min at 37 °C. Equivalent amounts of reaction mix, pellet, and supernatant fractions were loaded on a 12% SDS-polyacrylamide gel, and protein bands were visualized by Coomassie staining.

Surface Plasmon Resonance (SPR) Binding Assays—SPR binding experiments were performed on a Biacore 3000 instrument using CM5 sensor chips. Two different strategies for protein immobilization were used when working with antibodies and Xaperones, respectively.

The antibodies Abcam 187328 and mAb 1/108 were captured on the surface by a covalently immobilized anti-Fc antibody. Anti-rabbit Fc or anti-mouse Fc was used for Abcam 18732 or mAb 1/108. These capturing antibodies were immobilized via standard amine coupling chemistry. Captured anti-hDCX antibodies were cleaved off with 100 mM H_3PO_4 and fresh anti- hDCX antibody recaptured after each binding experiment. When working with Xaperones, either the hDCX or the Xaperone was covalently immobilized using standard amine coupling chemistry.

All binding experiments were performed in 10 mM HEPES, 150 mM NaCl, 3 mM EDTA, 0.01% P20, pH 7.4, to 7.6. Experiments were performed at 25 °C. A 1:1 binding model was fit to the recorded binding curves to extract the equilibrium and kinetic constants.

Analytical Ultracentrifugation (AUC)—A sample of 8 μM C-DCX (residues 251–356) was centrifuged at 42,000 rpm and 20 °C in 12-mm Epon charcoal-filled centerpieces on a Proteome Lab XLI analytical ultracentrifuge equipped with an An-60Ti rotor (Beckman Coulter). The partial specific volume of 0.74 ml/g was calculated from the amino acid sequence. The buffer was 25 mM HEPES/NaOH, pH 7.5, 100 mM NaCl, 5 mM DTT. Sedimentation velocity data (radial scans with interference optics) were analyzed with Sedfit (24), and sedimentation coefficient distributions with $s_{20,w}$ values corrected for buffer viscosity and density were plotted with GUSSI (25).

NMR Measurements and Assignment—The protein sample for the NMR studies contained 500 μM uniformly ^{15}N-^{13}C-labeled C-DCX in 20 mM sodium acetate (pH 4.0), 5 mM TCEP, and 5% D_2O. All of the NMR spectra were collected at 300 K on either a Varian Unity Inova 600-MHz spectrometer equipped with a triple resonance probe or a Bruker 600-MHz Avance II spectrometer equipped with a cryogenic TCI probe head. The backbone and aliphatic side chain resonances of C-DCX (^1H, ^{15}N, and ^{13}C) were assigned using a combination of experiments, including two-dimensional ^1H-^{15}N HSQC, three-dimensional HNCO, three-dimensional HNCACB, three-dimensional (HB)CBCA(CO)NNH, three-dimensional C(CO)NNH, three-dimensional HNCA, three-dimensional HN(CO)CA, and three-dimensional HN(CA)CO. Chemical shifts of the proton, carbon, and nitrogen nuclei were referenced externally to that of 4,4-dimethyl-4-silapentane-1-sulfonic acid at 0 ppm. NMR data were processed using the NMRPipe/NMRDraw package (26) and analyzed with NMRView (27). The ^1H, ^{13}C, and ^{15}N chemical shift assignment for C-DCX has been deposited in the BioMagnResBank under accession number 26727.

Crystallization and Structure Determination—For the crystallization of N-DCX_{DD} or SEC-purified heterodimeric complexes of T-DCX with Fab1/108 or C-DCX with XA4551, sitting drop plates in combination with various screens (Hampton Research) and temperatures were used. Crystallization droplets contained a 45 or 70% fraction of protein in a total volume of 400 nl. N-DCX_{DD} crystals were obtained out of either 20 mM CAPS, pH 10.5, 100 mM NaCl, 5 mM TCEP or 20 mM HEPES, pH 7.5, 100 mM NaCl, 5 mM DTT. For data collection, N-DCX_{DD} crystals were harvested directly from the screening plates without further optimization. Complex crystals of T-DCX with Fab1/108 grow out of 20 mM HEPES, pH 7.5, 100 mM NaCl, 5 mM DTT. The C-DCX XA4551 complex crystallized from 20% polyethylene glycol monomethyl ether, 100 mM BisTris, pH 6.5. Crystals obtained from C-DCX alone at pH 4 and at pH 10 did not yield a structure. All crystals of the DCX variants appeared within the first 4 days after setup with the exception of the Fab1/108 complex, where the first crystals were visible after several weeks. Crystals were harvested either without or with glycerol as cryoprotectant and then flash-cooled in liquid nitrogen.

All diffraction images were collected at a temperature of 100 K at the beam line X10SA (PXII) of the Swiss Light Source using a Pilatus pixel detector (Dectris). Images were processed with XDS (28) and scaled with SADABS (obtained from BRUKER AXS). All N-DCX data sets were phased by molecular replacement with either MOLREP or PHASER (29), initially using the coordinates of human N-DCX_{DD} (PDB entry 2BQQ) as the search model and later in-house N-DCX_{DD} coordinates of better resolution. Antibody search models were extracted from PDB entry 12E8 for the Fab and PDB entries 2X1O, 2X1P, 2X6M, 3DWT, 3EAK, 3G9A, and 3P0G for the V_{HH}. The Fab

and Xaperone CDRs could be easily traced using COOT (30). Attempts to determine the structures of C-DCX crystals by molecular replacement with DCX domains failed. However, for the C-DCX XA4551 complex crystals, molecular replacement with a V_{HH} ensemble search model resulted in electron density maps that allowed us to autobuild the DCX domain with ARP/wARP (31). The structures were refined with either BUSTER (32), REFMAC5 (33), or PHENIX (34). All structural modeling was performed with COOT (30), and the CCP4 program suite (35) was used for all other crystallographic calculations. Table 1 gives an overview on the structures and their quality.

Results

mAb 1/108 Binds N-DCX—The commercial doublecortin antibodies, such as the rabbit polyclonal Abcam 18732, are widely used for immunohistochemistry to detect brain neurogenesis and did bind to hDCX in Western blotting as advertised. However, Abcam 18732 failed to bind N-DCX, C-DCX, or T-DCX in Western blotting and in ELISA, indicating an epitope in the serine/proline-rich C-terminal region of doublecortin (Table 2). To obtain domain specific antibodies as tools for assessing doublecortin structure and function, we raised new mouse monoclonal antibodies against native human doublecortin that bind the protein in ELISA but not in Western blot experiments. Among the obtained antibodies, only mAb 1/108 formed a defined 1:1 complex with T-DCX, as determined by sedimentation velocity AUC (data not shown). The complex was soluble and did not show light scattering due to protein aggregation. Therefore, the mAb 1/108-derived Fab1/108 was selected for T-DCX co-crystallization. Binding of mAb 1/108 to N-DCX, T-DCX, and hDCX but not to C-DCX was observed in SPR experiments. The equilibrium binding constant (K_D) of Fab1/108 to hDCX was determined by SPR to be 27 nM (Table 2). The above results suggest that mAb 1/108 binds specifically the N-terminal domain of doublecortin and could be a unique research tool to distinguish the roles of individual DCX domains in doublecortin function.

The V_{HH} XA4551 Binds C-DCX—Because no antibody specific for C-DCX could be identified among the mouse clones raised against hDCX (data not shown), single chain camelid antibodies against T-DCX were raised in llamas. To generate tool antibodies for assessing C-DCX structure and function, the resulting V_{HH} cDNA libraries generated from the blood lymphocytes were panned for V_{HH} that bind C-DCX. XA4551 belongs to a panel of 12 V_{HH} clones, all showing a unique sequence, that bind both T-DCX and C-DCX in ELISA experiments. SPR assays revealed binding to hDCX, T-DCX, and C-DCX but not to N-DCX (Table 2). The binding constants of XA4551 to full-length doublecortin were determined by SPR analysis to be as follows when the XA4551 was immobilized and full-length doublecortin was present in the mobile phase: K_D = 29.8 nM ($k_{on} = 3.13 \times 10^6\ s^{-1}$, $k_{off} = 0.0931\ s^{-1}$). However, binding was weaker, with K_D = 451 nM ($k_{on} = 1.95 \times 10^5\ s^{-1}$, $k_{off} = 0.0881\ s^{-1}$) when hDCX was immobilized and XA4551 was present in the mobile phase. Random amine coupling of C-DCX to the surface chip may have hampered access of XA4551 to its epitope, resulting in apparently slower k_{on} and higher K_D, and indeed, the crystal structure showed four of the 10 lysines on the C-DCX surface available for amine coupling to be <8 Å from the XA4551 binding epitope (Lys^{255}, Lys^{274}, Lys^{283}, and Lys^{300}). Despite the relatively high dissociation constants measured by SPR, XA4551 formed stable complexes of 1:1 stoichiometry with C-DCX and T-DCX, as shown by a constant 1:1 molar ratio across the whole SEC peak when investigated with SEC/RP-HPLC and also by sedimentation velocity AUC (data not shown). In conclusion, camelid V_{HH} XA4551 binds specifically the C-DCX domain of doublecortin and could be a suitable research tool for C-DCX structure determination.

Effect of Domain-specific Antibodies on Microtubule Binding—To specify the role of the single DCX domains in doublecortin function, we assessed the effect of the domain-specific antibodies on microtubule binding and on tubulin polymerization. The doublecortin tandem domain construct T-DCX was able to bind taxol-stabilized microtubules in a microtubule pelleting assay, whereas isolated N-DCX and C-DCX domains did not bind microtubules, as expected from previous studies (5) (Fig. 1*a*). When added in equimolar concentrations, mAb 1/108 did not interfere with microtubule binding of T-DCX (Fig. 1*c*), whereas XA4551 disrupted T-DCX microtubule binding (Fig. 1*d*). This is consistent with other results derived from truncated doublecortin variants (5) but appears to be in conflict with ^1H-^{15}N HSQC NMR spectra showing substantial line broadening for both isolated N-DCX and C-DCX when incubated together with microtubules (7).

Crystal Structures of N-DCX_{DD} Show Variable Interactions of Trp^{227} with the Domain Core—The C-terminal region of N-DCX (residues 221–245), which links the N-DCX core with C-DCX and includes Trp^{227}, was proposed to play an important role in doublecortin function, because it mediates the conformational changes between open and closed doublecortin states (13). To further elucidate the conformations important for doublecortin function, crystal structures of N-DCX_{DD} were obtained in three novel crystal forms and were refined to resolutions between 2.48 and 1.3 Å (Table 1). The N-terminal cloning artifact sequence LVPRG, which is missing in the N-DCX_{DD} variant described previously (13), may explain why we obtained different crystals. And indeed it is involved in a crystal packing interaction in our hexagonal crystal form (PDB entry 5IOI). Despite the same space group, also the packing in our tetragonal crystals (PDB entry 5IN7) differs from the previously reported crystal (PDB entry 2BQQ). Because each of the three different crystals contained several molecules of N-DCX_{DD} in the crystallographic asymmetric unit, the structures of overall 10 independent N-DCX_{DD} chains are available for comparison. In all structures, N-DCX_{DD} assumes the typical ubiquitin-like fold of DCX domains (Fig. 2*a*). The residues 133–220 represent the core region that is well ordered in all structures and correspond well to the generic DCX domain (residues 129–220) as defined by the SMART database (36). This core region is virtually identical in all N-DCX_{DD} structures (main chain root mean square (r.m.s.) distances of 0.7–1.2 Å). By contrast, the observed conformation of the C-terminal residues 221–231 differs drastically (Fig. 2). In two of the 10 N-DCX_{DD} chains, this C-terminal region is disordered, and residues 221–231 are excluded in the respective model (Table 1). Among the remaining eight N-DCX_{DD} structures, three conformations of the

TABLE 1
X-ray data collection and refinement statistics

Structure	N-DCX$_{DD}$	N-DCX$_{DD}$	N-DCX$_{DD}$	N-DCX·Fab1/108	C-DCX·XA4551
PDB code	5IN7	5IO9	5IOI	5IKC	5IP4
Data collection					
Space group	I422	P1	P6$_1$22	P2$_1$	C2
Copies/asymmetric unit	2	2	6	2	2
Cell *a*, *b*, *c* (Å)	82, 82, 140	27, 38, 48	98, 98, 377	67, 110, 75	90, 86, 73
Cell α, β, γ (degrees)	90, 90, 90	89, 106, 97	90, 90, 120	90, 106.5, 90	90, 123, 90
Solvent content (%)	53	41	68	48	56
Resolution (Å)	45–2.48 (2.55–2.48)[a]	26–1.3 (1.40–1.30)	35–2.4 (2.50–2.40)	42–2.06 (2.13–2.06)	44.8–1.81 (1.90–1.81)
No. of reflections (total)	13,425 (672)	39,993 (6149)	79,206 (9137)	215,011 (19,951)	146,061 (13,750)
Multiplicity	12.9 (13.0)	1.9 (1.4)	11.6 (11.0)	3.4 (3.2)	3.4 (3.3)
Completeness (%)	99.9 (99.8)	85.7 (66.5)	99.9 (99.9)	99.2 (97.8)	99.8 (99.7)
R_{MEAS}[b]	14.6 (125)	5.5 (61)	14.7 (110)	19.2 (230)	7.7 (110)
$CC_{½}$[b]	1.0 (0.77)	1.0 (0.7)	1.0 (0.85)	0.99 (0.3)	1.0 (0.45)
$I/\sigma(I)$	9.6 (2.7)	10.9 (2.2)	15.6 (2.7)	7.3 (1.0)	10.3 (1.3)
Wilson *B*-value	63.0	13.8	55.1	30.1	37.4
Refinement	BUSTER	BUSTER	BUSTER	PHENIX	REFMAC5
Resolution (Å)	45–2.48 (2.77–2.48)	26–1.3 (1.33–1.30)	35–2.4 (2.46–2.40)	42–2.06 (2.13–2.06)	44.8–1.81 (1.86–1.81)
R_{cryst} (%)	19.8 (24.4)	18.8 (26.0)	19.8 (25.0)	19.7 (36.0)	19.7 (41.8)
R_{free} (%)	23.7 (34.4)	21.0 (26.2)	23.4 (26.0)	26.3 (42.4)	24.6 (44.8)
Completeness (%)	99.9 (99.9)	89.9 (89.9)	99.9 (99.9)	99.2 (97.8)	96.0 (87.1)
DCX residue range crystallized	126–231	133–231 plus 125–132 artefact	133–231 plus 125–132 artefact	126–356	251–341
Residues in refined model	A: 132–231; B: 132–227	A: 132–229; B: 133–230	A: 125–231; B: 133–220; C: 133–228; D: 132–220; E: 125–231; F: 133–227	M: 132–220; N: 132–221	D: 255–334; E: 255–338
r.m.s. deviation, bonds (Å)	0.01	0.013	0.01	0.009	0.019
r.m.s. deviation, angles (degrees)	1.13	1.15	1.14	1.17	2.121
Ramachandran quality (PROCHECK core/disallowed)	93.1/0.0	90.1/0.0	90.6/0.0	89.6/0.6	90.4/0.0
Mean *B*-value protein atoms	52.4	19.1	49.0	42.1	31.6

[a] Values in parentheses are for the highest resolution range.
[b] *R* values and $CC_{½}$ are defined in Refs. 39 and 40.

TABLE 2

Binding analysis

SPR, surface plasmon resonance on a Biacore instrument with the DCX variant immobilized. WB, Western blot. +, −, and ND, binding, not binding, and not determined, respectively. If a K_D value was determined, it is given. The value in parentheses is from an inverse setup, with the XA4551 immobilized on the SPR chip and the hDCX in the mobile phase.

	Abcam 18732 (SPR)	Abcam 18732 (WB)	XA 4551 (SPR)	XA 4551 (WB)	XA 4551 (ELISA)	mAb 1/108 (SPR)	mAb 1/108 (WB)	mAb 1/108 (ELISA)
hDCX	+	+	+	−	+	+	−	+
	1 nM[a]		451 nM (30 nM)			27 nM		
T- DCX	−	−	+	ND	+	+	ND	ND
N-DCX	−	−	−	ND	ND	+	Weak	ND
C-DCX	−	−	+	ND	+	−	Very weak	ND

[a] Estimated apparent K_D. The SPR binding curve cannot be fitted with a 1:1 binding model, as expected for a polyclonal antibody mix.

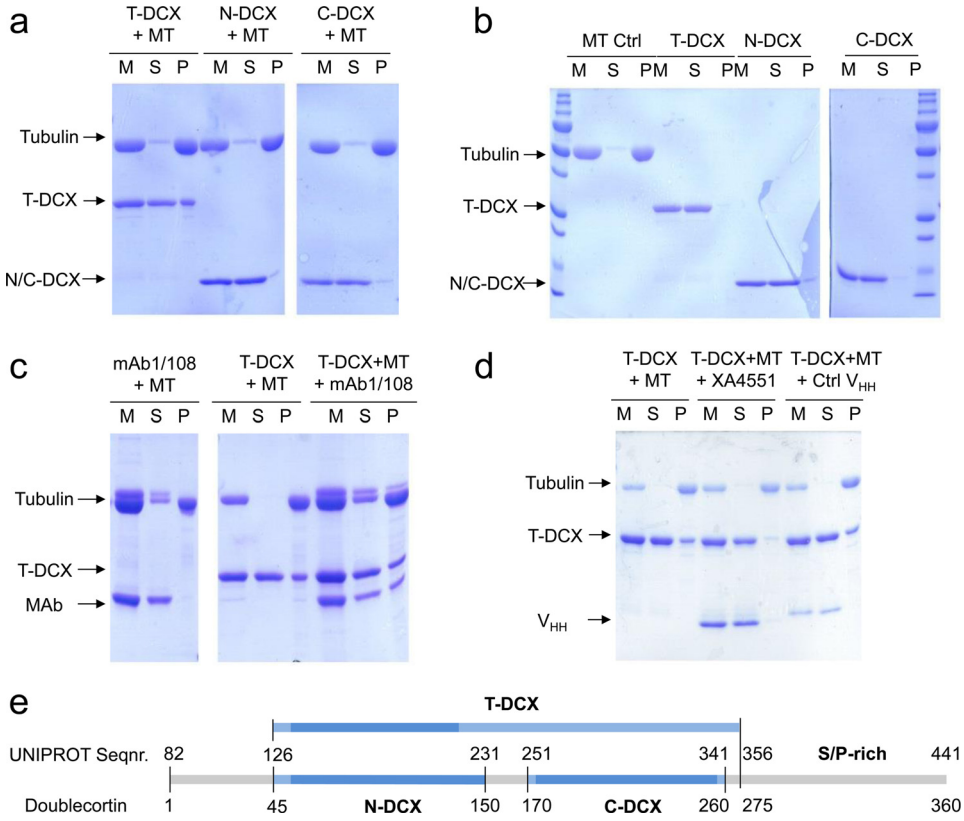

FIGURE 1. **Effect of doublecortin-specific antibodies on doublecortin binding to microtubules and on tubulin polymerization.** *a*, the doublecortin variant with the complete domain tandem T-DCX co-pelleted with taxol-stabilized microtubules in a microtubule pelleting assay, whereas isolated N-DCX and C-DCX domains did not (*M*, reaction mix; *S*, supernatant; *P*, pellet; *MT*, microtubule). *b*, the controls show that the faint bands of N-DCX and C-DCX observed in the pellet are independent of microtubules. *c*, the N-DCX-specific antibody mAb 1/108 co-pelleted with T-DCX and microtubules while showing no effect on binding of DCX to microtubule. mAb 1/108 did not co-pellet with microtubule alone. *d*, the addition of the C-DCX-specific Nanobody XA4551 inhibited co-pelleting of T-DCX with microtubules. A control (*Ctr*) Xaperone not binding doublecortin had no effect on microtubule binding of T-DCX. *e*, overview of doublecortin domain arrangement. Construct boundaries for N-DCX, C-DCX, and T-DCX are given in both the UNIPROT numbering scheme used in this study and in the numbering used in some other doublecortin publications.

C-terminal peptide are observed that are distinct from those described previously (7, 13). Despite the large differences in the main chain trace of the N-DCX C-terminal residues, the side chain of Trp^{227} always stacks against the side chain of Arg^{137} and interacts with Val^{150} of the N-DCX core (Fig. 2). This interaction is intramolecular in PDB entries 5IO9 and 5IN7 and chains C and F of PDB entry 5IOI, whereas in chains A and E of PDB entry 5IOI, Trp^{227} stacks against Arg^{137} of a crystal lattice neighbor in an intermolecular interaction. Thus, the novel structures of $N\text{-}DCX_{DD}$ include the first x-ray structures in the closed conformation and illustrate the full conformational space that is available to the C-terminal region of the N-DCX domain. Conformational changes in region 221–245 are proposed to modulate the doublecortin domain arrangement in microtubule binding, and our structures hint at a critical role of Trp^{227} in controlling this conformational switch.

Wild Type N-DCX Crystal Structure in Complex with Fab1/108 Confirms $N\text{-}DCX_{DD}$ Structures—To gain insight into the architecture of the DCX tandem domains, the complex of T-DCX with the Fab1/108 was set up for crystallization. After 2 months, a crystal appeared. Two copies of a complex of N-DCX core residues with Fab1/108 could be unambiguously placed into the crystallographic asymmetric unit, but no electron density for C-DCX could be located. Furthermore, the crystal packing provides no space for two additional C-DCX domains, and the solvent content calculated from the model is in the normal range (48%). The absence of residues C-terminal of Thr^{220} in both N-DCX molecules in this crystal is consistent with the

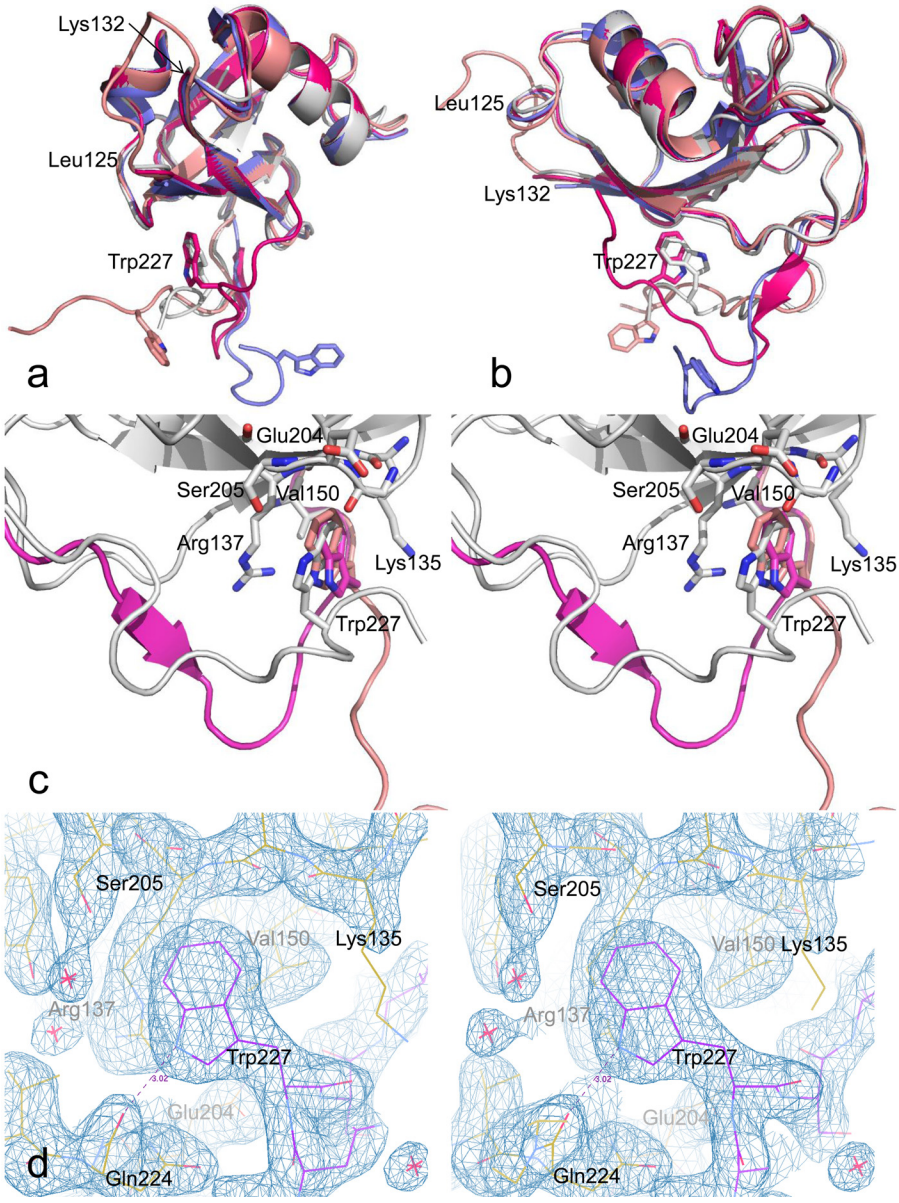

FIGURE 2. **The high resolution structures of N-DCX illustrate the different conformations occupied by its mobile C-terminal region.** *a*, a superposition of three N-DCX structures from different crystals (chain A of 5IO9 *colored light gray*; chain E of 5IOI *colored pink*; chain A of 5IN7 *colored magenta*) onto PDB entry 2BQQ (7) (*colored blue*) shows new open and closed N-DCX conformations. *b*, the superposition shown in *a* but rotated by 90° around the *vertical axis*. *c*, despite the big differences in open and closed conformations of the C-terminal region, Trp^{227} always contacts a shallow pocket created by residues Lys^{135}, Val^{136}, Arg^{137}, Gly^{203}, Glu^{204}, and Ser^{205} on the DCX core. In the open conformation observed in 5IOI, this contact is intermolecular, Trp^{227} binding the pocket on a crystal neighbor. *d*, *stereo image* showing the $2F_o - F_c$ electron density at 1σ and 5IOI chain E Trp^{277} (*magenta*) interacting with Lys^{135}, Val^{136}, Arg^{137}, Gly^{203}, Glu^{204}, and Ser^{205} of chain A (*yellow*).

observation of multiple distinct conformations of this region in our $N\text{-}DCX_{DD}$ structures. The inherent flexibility in this region probably allowed a contaminating protease to cleave T-DCX. Hence, comparing the conformation of the C-terminal peptide 222–245 of wild type N-DCX with those observed in $N\text{-}DCX_{DD}$ was not possible. The structure of the human wild type N-DCX domain core when bound to the antibody is virtually identical to the isolated $N\text{-}DCX_{DD}$ domain and can be superimposed on the various $N\text{-}DCX_{DD}$ structures with r.m.s. distances ranging from 0.5 to 1.0 Å (Fig. 3*a*). This result demonstrates that the surface entropy-reducing double mutation K214D/K215D introduced for crystallization did not affect the conformation of the N-DCX core. Fab1/108 recognizes the N-DCX loops 142–146, 174–177, and 213–216. N-DCX residue Ile^{176} binds deeply into a cleft between the two CDR3 of the light and heavy chains, mainly interacting with the aliphatic atoms of heavy chain Lys^{100} and Arg^{50} and with light chain Tyr^{94}. N-DCX Tyr^{145} has an aromatic stacking interaction with light chain Tyr^{49}. N-DCX Asp^{143}, Arg^{144}, Tyr^{145}, and Lys^{215} are hydrogen-bonded to Fab1/108, and N-DCX Phe^{213} and Val^{217} make additional hydrophobic contacts (Fig. 3). It is noteworthy that the Lys^{215} side chain that is mutated to Asp in the $N\text{-}DCX_{DD}$ that was specially designed for crystallization is also part of the epitope recognized by the crystallization helper Fab1/108. This first structure of wild type N-DCX

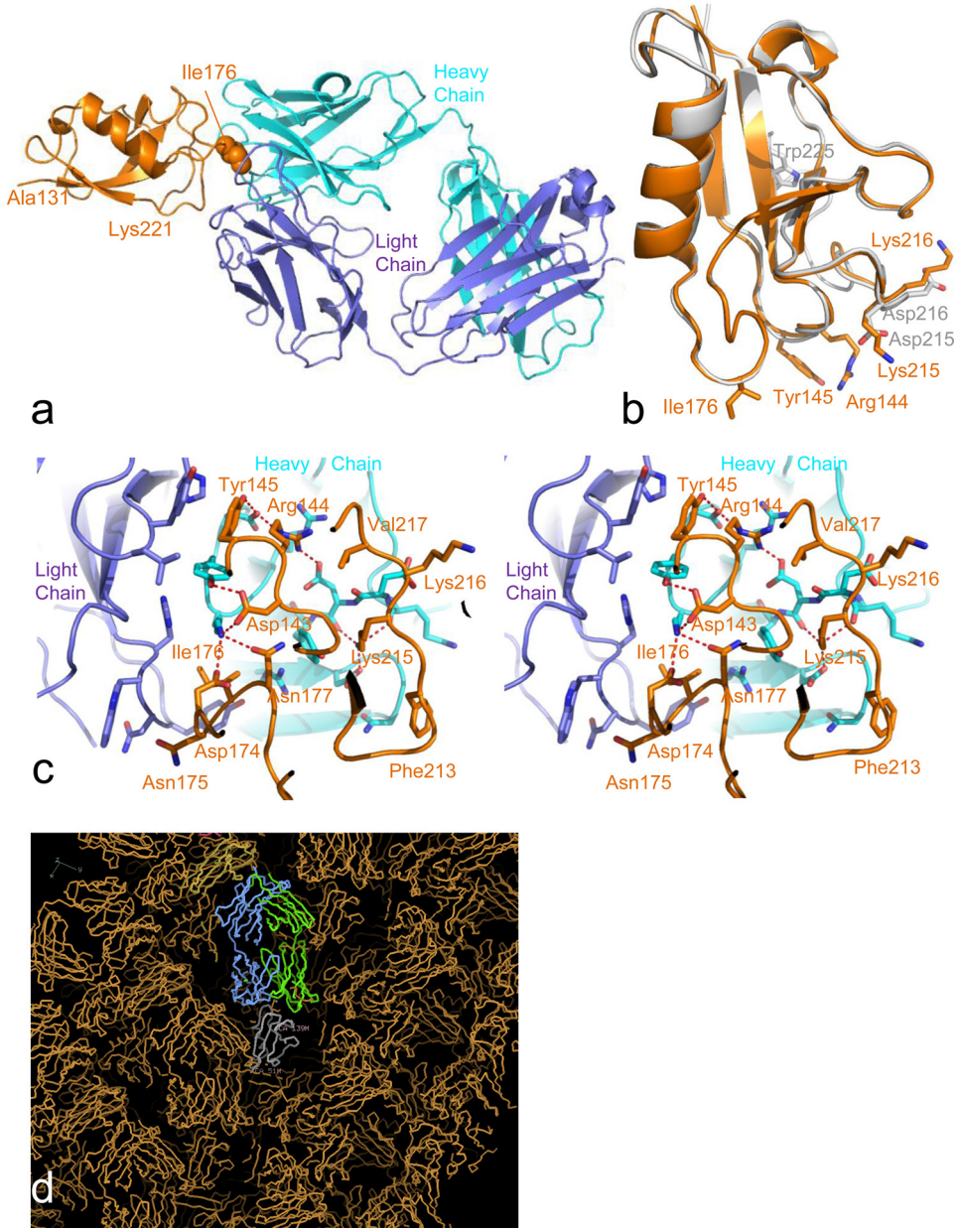

FIGURE 3. **The complex of wild type N-DCX with Fab1/108.** *a*, schematic of the complex, N-DCX *colored orange*, Fab light chain *colored blue*, and heavy chain *colored cyan*. N-DCX Ile^{176} at the center of the antibody epitope is highlighted in a *ball representation*. *b*, superposition of wild type N-DCX (*orange*) onto N-DCX$_{DD}$ (*gray*) shows that the double mutation K215D/K216D introduced for crystallization did not disturb the DCX core structure in N-DCX$_{DD}$. The side chains of other residues interacting with the Fab1/108 are also shown. *c*, *stereo image* of the binding interface shows how Fab1/108 wraps around Ile^{176} with the hydrophobic atoms of Lys^{100} and Arg^{50} from heavy chain and Tyr^{94} and His^{91} from light chain. Additionally, N-DCX Asp^{143}, Arg^{144}, Tyr^{145}, Asp^{174}, Asn^{177}, and Lys^{215} are hydrogen-bonded to Fab1/108, and Phe^{213} and Val^{217} make hydrophobic contacts. Notably, Lys^{215} of the K215D/K216D crystallization mutation in N-DCX$_{DD}$ is part of the epitope recognized by the crystallization helper Fab1/108. *d*, the crystal packing is dense, without voids that would provide space for the C-DCX domain.

confirms the validity of using the structural information obtained from the N-DCX$_{DD}$ variant and also serves to determine the epitope of the new N-DCX-specific mAb 1/108 research tool.

C-DCX Shows Cooperative Thermal Unfolding—To identify optimal protein formulations for structural studies, C-DCX (residues 251–356) was subjected to a thermofluor screen (14). In the buffer 125 mM NaAc, pH 4.5, 400 mM NaCl, and 180 mM CAPS, pH 10.0, 400 mM NaCl C-DCX displayed cooperative unfolding transitions with melting temperatures of 59 and 68 °C, respectively. At more neutral pH (*e.g.* 180 mM Hepes, pH 7.0, 400 mM NaCl), Sypro Orange fluorescence was already present at ambient temperature, indicating an exposed hydrophobic surface; hence, no melting temperature could be detected (Fig. 4*a*). The protein was therefore stored in sodium acetate buffer, pH 4, or CAPS buffer, pH 10.5, for subsequent structural analysis.

NMR Shows Isolated C-DCX to Assume the DCX Fold in Solution—To characterize the solution structure of C-DCX, NMR experiments were conducted. Two-dimensional ^{1}H-^{15}N HSQC NMR spectra of C-DCX obtained at almost neutral pH showed broad peaks indicative of protein aggregation. In con-

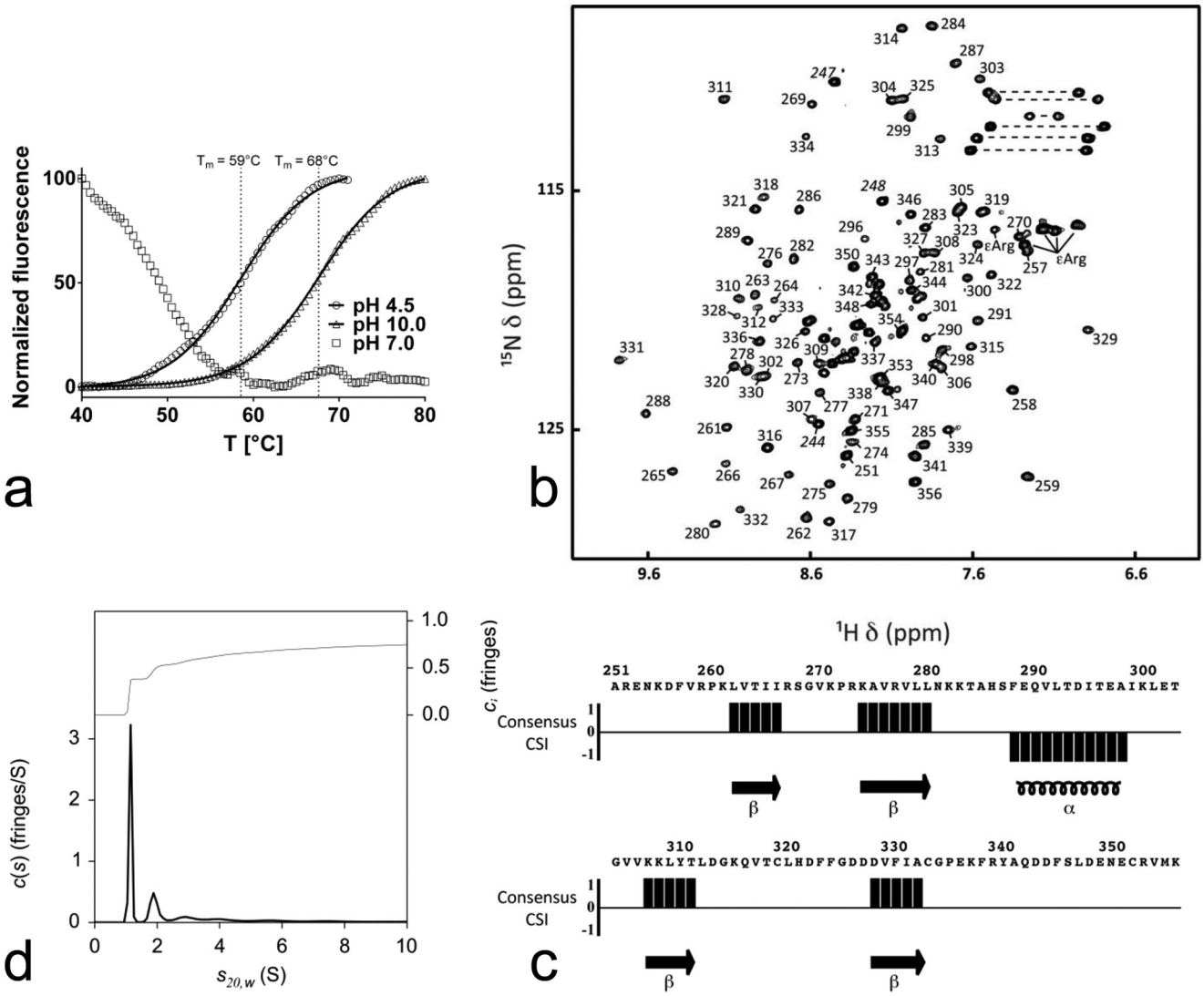

FIGURE 4. **C-DCX assumes an ordered structure.** *a*, thermal shift curves from the thermofluor buffer screening show thermal unfolding transitions for C-DCX in the buffers 125 mM NaAc, pH 4.5, 400 mM NaCl (*blue*) and 180 mM CAPS, pH 10.0, 400 mM NaCl (*red*), whereas in 180 mM Hepes, pH 7.0, 400 mM NaCl (*green*), fluorescence is already present at the start and decays with protein precipitation. *b*, the assigned two-dimensional ^{1}H-^{15}N HSQC spectrum of C-DCX in NMR buffer at 300 K and pH 4. Additional residues at the N terminus (residues 244–250) are due to a cloning artifact. *c*, chemical shift index (*CSI*) histogram shows the predicted secondary structure for C-DCX to be consistent with the DCX fold. Consensus CSI values of −1 indicate α-helix, whereas values of 1 correspond to β-strand structures. *d*, sedimentation coefficient distribution $c(s_{20,w})$ for C-DCX at pH 7.5 reveals a dominant monomer peak at 1.15 S, which is consistent with a folded DCX domain. The *top panel* with the integrated distribution shows that the monomer peak comprises 48% of the total loading signal and a series of oligomers accounts for the rest.

trast, the NMR spectrum obtained in sodium acetate at pH 4 showed sharp peaks and high dispersion both in the ^{1}H and ^{15}N chemical shift dimensions, indicating that C-DCX assumes a defined structure at pH 4 (Fig. 4*b*). The data quality allowed the complete assignment of the backbone nuclei (^{1}HN, ^{15}N, $^{13}C\alpha$, and $^{13}C\beta$) and partial assignment of the side chain heavy atoms for residues 251–356 of C-DCX. The secondary structure of C-DCX was predicted by the chemical shift index (37), based on the chemical shifts for the $^{13}C\alpha$, $^{13}C'$, and $^{13}C\beta$ nuclei. The chemical shift index method predicted one α-helix between residues 288 and 298 and four β-strands between residues 262 and 266, 274 and 280, 307 and 311, and 328 and 332 (Fig. 4*c*). These secondary structure elements are consistent with C-DCX assuming the archetypical ubiquitin-like fold of other DCX domains. After the crystal of the C-DCX XA4551 complex became available, no further structure determination by NMR was attempted.

AUC Sedimentation Data of C-DCX at pH 7.5 Indicate a Folded Structure—To study the behavior of C-DCX at more neutral pH, C-DCX was analyzed by AUC in HEPES buffer at pH 7.5. The sedimentation coefficient distribution, $c(s)$, shows a dominant peak at $s_{20,w} = 1.15$ S that comprises 48% of the total loading signal (Fig. 4*d*). This peak belongs to the monomer of C-DCX (residues 251–356), and the peaks at $s_{20,w} > 1.5$ S correspond to oligomers. Despite the sample heterogeneity, the molecular mass of 12.1 kDa calculated from the $s_{20,w}$ for the main species is within 93% of the molecular mass expected from the C-DCX amino acid sequence (13.0 kDa).

For sedimentation data, the observed frictional ratio f_h/f_0, a low resolution descriptor of shape or particle asymmetry,

equals the ratio of radii, r_h/r_0. The subscript h denotes the Stokes frictional coefficient and the Stokes radius of the actual protein, whereas the subscript 0 denotes the value for an equivalent sphere with the same mass and density. From the sedimentation data of the dominant peak, a frictional ratio of $f_h/f_0 = 1.56$ is fitted, which translates into $r_h = 2.42$ nm and $r_0 = 1.52$ nm. These values are consistent with C-DCX having at pH 7.5 a compact, folded DCX core domain structure with flexible terminal extensions as opposed to a molten globule.

Crystal Structure of C-DCX in Complex with XA4551 Confirms Its DCX Fold—For crystallization, a complex of C-DCX and the V_{HH} XA4551 in 20 mM CAPS, pH 10.5, was purified by SEC and mixed with 20% polyethylene glycol monomethyl ether, 100 mM BisTris, pH 6.5, as precipitant, resulting in pH 6.5 in the crystallization droplet. The data set to 1.81 Å resolution collected from the obtained crystal was used to solve the structure of the complex (Table 1). C-DCX core residues 255–324 are defined in the electron density. As expected from the sequence and from our NMR results, C-DCX assumes the archetypical DCX fold (Fig. 5*a*). When superimposed on the NMR structure of the C-terminal DCX domain of DCDC2 that shares 32% sequence identity with C-DCX (PDB entry 2DNF), the resulting r.m.s. distance is 1.9 Å (Fig. 5*b*). The C-DCX structure superimposes equally well on N-DCX with r.m.s. distances ranging from 1.9 to 2.3 Å between C-DCX and the 10 different N-DCX chains available for comparison. The regions with the largest differences compared with N-DCX are the loops around residues 303 and 271 (Fig. 5*c*). The V_{HH} XA4551 recognizes mainly the surface-exposed residues on the β-strand 276–280 and on the α-helix 291–298 as well as on the loop connecting them and the neighboring loop 260–262 (Fig. 5, *a* and *e*). This epitope on C-DCX comprises a hydrophobic surface that includes a shallow groove exposing aliphatic side chain atoms of residues Val^{276}, Val^{278}, Leu^{280}, Ala^{285}, Ile^{295}, and Val^{291}. The corresponding residues in N-DCX and N-doublecortin-like kinase domains are deeply buried in the hydrophobic core by the Phe^{158} side chain emerging from a neighboring loop (Fig. 5, *d* and *e*). The paratope on XA4551 consists mainly of framework 1 and CDR1 residues, with Ile^{31} from CDR1 filling the hydrophobic groove on C-DCX. No residue from CDR3 and only 2 residues from CDR2 and framework 3 interact with C-DCX (Fig. 5*e*).

Discussion

A conformational switching model between an open and a closed conformation of doublecortin was previously proposed with the sequence region 221–245 that connects the DCX domains expanding or folding back on the N-DCX core and thereby modulating the distance between the N-DCX and C-DCX domains (13). This model postulates that the resulting changes in the distance between N-DCX and C-DCX are of functional importance in the control of tubulin polymerization and microtubule bundling. The model was based on three independent observations on three different proteins. 1) A closed doublecortin conformation was observed in the NMR structure of N-DCX characterized by an intramolecular interaction of Trp^{227} with Arg^{137}. 2) Also, a similar molecular interaction between Trp^{150} and the aliphatic part of Arg^{60} is present in the crystal structure of doublecortin-like kinase N-terminal DCX domain (7). 3) The only observation of an open conformation was in the one x-ray structure of $N\text{-}DCX_{DD}$ (PDB entry 2BQQ). However, there the extended C-terminal region of the doublecortin N-DCX domain had extensive contacts with its crystal neighbor molecule across a crystallographic 2-fold axis, which stabilized the extended conformation (13).

With the 10 independent N-DCX domain structures discussed here, we provide more evidence corroborating and extending the conformational switching model of doublecortin function. The C-terminal region folds back onto the N-DCX domain core, and the side chain of Trp^{227} contacts Arg^{137} in an intramolecular interaction in the $N\text{-}DCX_{DD}$ PDB entries 5IO9 and 5IN7 and in chains C and F of 5IOI, which therefore confirm the closed doublecortin conformations (Fig. 2). A closed conformation derived from the NMR structure of N-DCX was also used to fit the doublecortin density at the vertex of four tubulin dimers in microtubules observed in cryo-EM (8, 10). In PDB entry 5IOI chains A and E, the C-terminal sequence regions are observed in an extended open conformation (Fig. 2). Because Trp^{227} in 5IOI is interacting intermolecularly with Arg^{137} of a crystal lattice neighbor (Fig. 2*c*), we cannot rule out the possibility that also our experimentally observed open conformation is stabilized by the crystal lattice. A high conformational freedom of the C-terminal region of N-DCX is also indicated by the proteolytic cleavage of T-DCX that led to the wild type N-DCX Fab1/108 crystal. Also, the absence of the C-terminal linker region in 2 of 10 observed N-DCX copies in our crystals could be explained by conformational heterogeneity. Taken together, the differences in the trace of the C-terminal regions of the N-DCX crystal structures and the observation of three distinct closed conformations and two distinct open conformations in DCX domains suggest that each state in the conformational switch model of doublecortin function may comprise an ensemble of several conformations.

The minimal doublecortin fragment needed for co-assembly with microtubules in pelleting assays was T-DCX, and the $^{1}H\text{-}^{15}N$ HSQC NMR spectra of both N-DCX and C-DCX showed line broadening consistent with binding, when incubated with microtubules (5, 7). Also, patient mutations on both domains weakened the cooperative binding of doublecortin to 13-protofilament microtubules in fluorescence microscopy assays (11). However, in all cryo-EM structures of doublecortin bound to 13-protofilament microtubules, only one of the two DCX domains was observed at the corner of four tubulin dimers (8–10). Even from careful mapping and structural classification of X-linked lissencephaly and subcortical band heterotopia patient mutations onto this structure, the identity of this DCX domain, N-DCX or C-DCX, could not be unambiguously determined (6, 8). From these cryo-EM maps at ~8 Å resolution, distinction of the structurally similar N-DCX or C-DCX domains by their sequence alone is not possible. Actually, all C-DCX and N-DCX core domain coordinates resulting from the present study could be fitted into the density. In one cryo-EM study, additional density was visible C-terminal of the DCX domain core and reminiscent of the interaction with Trp^{227} observed in the structures of N-DCX assuming the

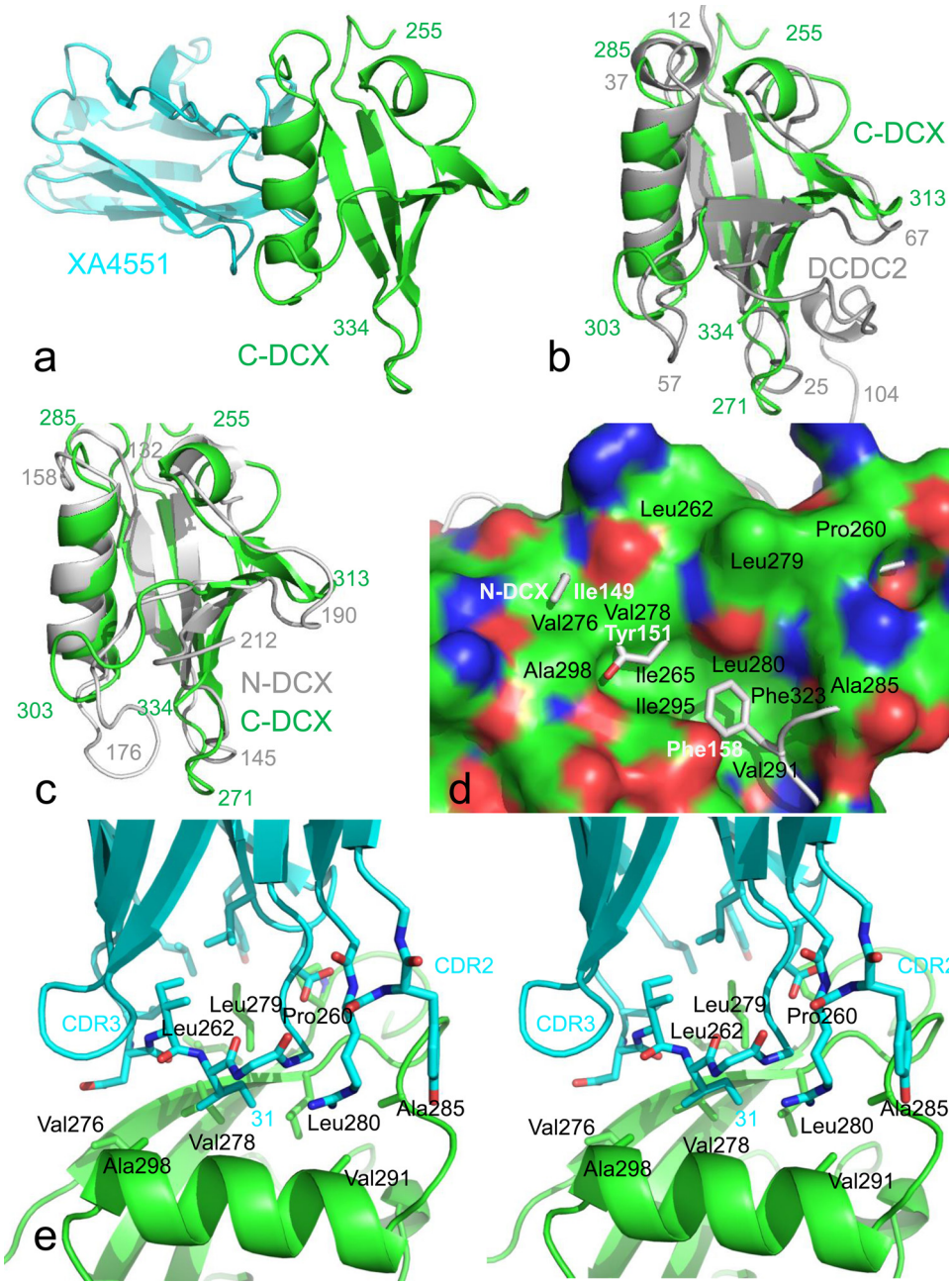

FIGURE 5. **The C-terminal DCX domain has the DCX fold.** *a*, overview of the complex between C-DCX (*green*) and the V_{HH} XA4551 (*cyan*). The orientation is the same as in *b* and *c*. *b*, superposition of the C-DCX domain (*green*) on DCDC2 C-terminal domain NMR structure (PDB entry 2DNF) (*dark gray*) shows that both assume the classical DCX fold. The N and C termini as well as a few surface loops are *labeled* with *residue numbers*. *c*, superposition of the C-DCX domain (*green*) on N-DCX core (*gray*). *d*, the hydrophobic surface patch on C-DCX (*green*) that is recognized by XA4551. *Black labels* indicate the C-DCX residues contributing to the hydrophobic surface. Superimposed is the structure of N-DCX (*gray*), where Tyr^{151} and Phe^{158} side chains prevent the formation of a hydrophobic surface pocket. *e*, *stereo image* showing how XA4551 (*cyan*) binds its epitope, which is a cluster of aliphatic side chains on the C-DCX surface on a β-strand-loop-helix motif (residues 276–298) and on an adjacent loop (residues 260–262). Ile^{31} of XA4551 CDR1 plugs a shallow pocket lined exclusively by aliphatic side chains.

closed conformation. Based on the similarity to closed N-DCX and the structural difference from the C-terminal DCX domain of the distant homolog DCDC2, it appeared reasonable to assign the domain bound to microtubules as N-DCX (10), although the main chain trace around Trp^{227} fitted the observed density only poorly. Later it was observed that only doublecortin patient mutations on C-DCX and not N-DCX affected binding to curved microtubules in single molecule fluorescence microscopy experiments, and all of those mutations (R259L, P272R, T303I, and G304E) are interacting with microtubules when the DCX domain in the cryo-EM is modeled as C-DCX (Fig. 6*b*) (12). And indeed, our data also indicate C-DCX to be the domain bound to microtubules in the cryo-EM studies, as will be detailed below.

Only the C-DCX-specific XA4551 disrupted T-DCX microtubule binding, whereas the N-DCX-specific Fab1/108 did not (Fig. 1, *c* and *d*). Because antibody binding did not alter the DCX domain structures (Figs. 3*b* and 5*b*), we assume that neither antibody induces a significant conformational change in doublecortin that prevents its binding to microtubules. A steric

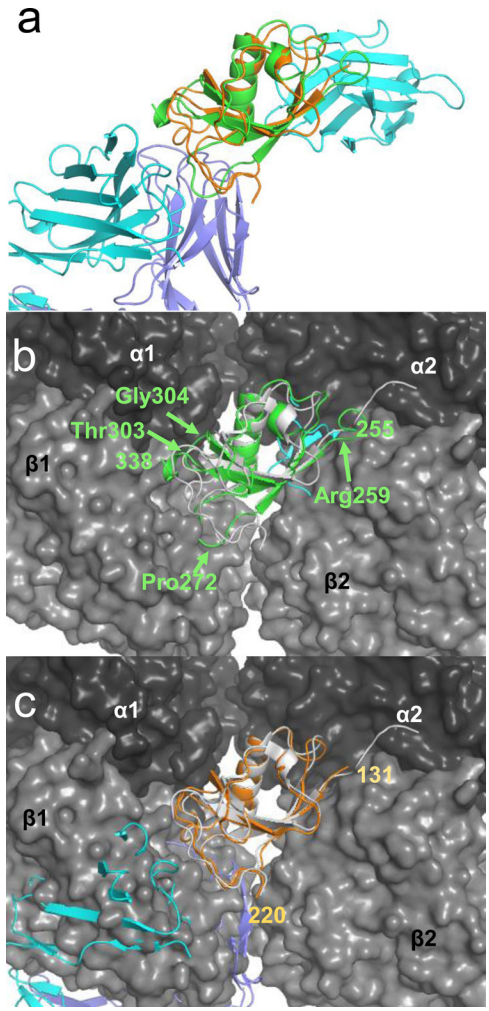

FIGURE 6. **The binding of anti-DCX domain antibody complexes is incompatible with the cryo-EM-derived binding mode of a DCX domain to 13-protofilament microtubules.** *a*, superposition of the DCX domains in the C-DCX XA4551 complex and the N-DCX Fab1/108 complex shows that the two antibodies recognize epitopes on different regions of the DCX domain fold (N-DCX *orange*, C-DCX *green*, antibodies *cyan* and *blue*). The DCX domains are in the same orientation as in *b* and *c*. *b*, superposition of the C-DCX·XA4551 complex on the DCX domain observed in the doublecortin microtubule complex PDB entry 2XRP shows that XA4551 clashes with tubulin α2 and β2. The location of the patient mutations R259L, P272R, T303I, and G304E that affected doublecortin binding to curved microtubules in single molecule fluorescence microscopy experiments is indicated by *arrows*. *c*, the same superposition of the N-DCX·Fab1/108 complex shows that Fab1/108 clashes with tubulin α1.

clash between DCX-bound antibody and the microtubule is therefore needed to prevent T-DCX from microtubule binding. If the antibody inhibits microtubule binding by steric clash, we can deduce that the regions of C-DCX interacting with microtubule include the XA4551 epitope. By similar reasoning, the N-DCX region in contact with Fab1/108 cannot be part of the microtubule binding interface. The superposition of the N-DCX and C-DCX antibody complexes with the DCX domain found in the cryo-EM structure showed that both XA4551 and Fab1/108 would clash with the microtubule lattice (Fig. 6). If N-DCX interacted with microtubules in the geometry observed in the cryo-EM reconstructions, Fab1/108 should prevent T-DCX from co-pelleting, which is not the case (Fig. 1*c*). Because only the C-DCX-specific XA4551 prevented T-DCX from co-pelleting with microtubules (Fig. 1*d*), the DCX domain observed in the cryo-EM density is very likely the C-DCX domain, although direct interaction of N-DCX with microtubules in a different binding geometry cannot be ruled out. If mAb 1/108 bound to a surface of N-DCX facing away from microtubules, it would not prevent co-pelleting of T-DCX with microtubules, even when N-DCX formed part of the binding interface to microtubules. Conformational heterogeneity of N-DCX could have led to loss of electron density for this domain during cryo-EM image processing and averaging. Future cryo-EM studies can use the DCX domain-specific antibodies described here as markers to distinguish the two DCX domains.

The isolated C-DCX domain was previously assigned to have molten globule-like properties, solely based on the recovery of ANS fluorescence ambient temperature and neutral pH and the extensive Stokes radius calculated from SEC retention times. But already the same study detected reasonably wide chemical shift dispersion of the C-DCX HSQC spectrum obtained at pH 7, and only the line broadening prevented NMR structure determination (7). C-DCX did not show all of the required hallmarks of molten globules, which include poor amide signal dispersion and rapid H_1D exchange, and indeed, we observed C-DCX to be a soluble and monodisperse monomer by SEC and AUC, showing cooperative thermal denaturation in Sypro Orange thermofluor assays at pH 4.5 and 10. Also, the AUC experiment at pH 7.5 yielded values for the Stokes frictional coefficient and radius that are consistent with a compact, folded DCX core domain structure with flexible terminal extensions (Fig. 4). Both the NMR assignment at pH 4 and the x-ray structure at pH 6.5 now showed that C-DCX assumes a defined structure with DCX fold. The hydrophobic surface pocket on C-DCX exposing several aliphatic side chains may explain the quenching of ANS and Sypro Orange fluorescence at neutral pH, although it does not explain why there is no quenching observed at acidic or basic pH.

Binding of XA4551 to this hydrophobic patch may indicate that this part of the C-DCX surface may be predisposed for protein-protein interactions. Such extended hydrophobic regions on globular proteins are characteristic for permanent protein-protein interfaces but are less often observed in transient protein-protein interactions, which instead frequently involve hydrogen bonds from side chains (38). N-DCX appears as the most obvious partner for a functionally important permanent intramolecular protein-protein interaction. However, this seems unlikely, because NMR data did not reveal any significant interaction between the two DCX domains within a tandem construct (7). In agreement with this view, isolated C-DCX and N-DCX did not form a stable complex, as judged by SEC (data not shown). Also, the N-DCX domain neither prevented ANS from binding to T-DCX nor protected the C-DCX domain from cleavage by contaminating proteases during crystallization of T-DCX. Superposition of C-DCX with the doublecortin domain bound to microtubules showed that the hydrophobic surface recognized by XA4551 is oriented toward the microtubule. This indicates a possible role of this hydrophobic patch in the transient protein-protein interaction with the microtubule lattice (Fig. 6).

In summary, this study presents the first high resolution structure of human C-DCX and the first crystallographic observation of closed conformations of the peptide region that links doublecortin N-DCX domain core to C-DCX. The C-DCX-specific antibody fragment XA4551 prevented co-assembly of T-DCX with microtubules, whereas the N-DCX-specific antibody mAb 1/108 did not. When overlaid on the microtubule-bound DCX domain observed in cryo-EM structures, the crystal structures of the antibody complexes suggest this domain to be C-DCX. Although the results presented here are in agreement with most previous data in the literature, their straightforward interpretation is incompatible with a substantial part of the current theories on doublecortin molecular mode of action. Full clarification of this apparent paradox will require further work in the future that may result in a new appreciation of the role of the C-DCX domain in doublecortin function.

Author Contributions—A. Ruf and R. T. conceptualized the study. A. Ruf determined the N-DCXDD and C-DCX crystal structures, coordinated all activities, and wrote the manuscript. J. B. and M. S. crystallized all proteins. D. B. and R. T. designed DCX constructs and produced, purified, and characterized all proteins. A. C. R. and B. D. designed and performed the C-DCX stability screen. M. D., T. L., and J. S. raised and selected the camelid V_{HH}. P. D. L., A. Ross, and D. F. performed, analyzed, and interpreted NMR experiments. W. H. designed, performed, and analyzed the SPR binding experiments. T. K. and G. S. contributed to study conception and experiment design. H. M. raised and selected the mAb. M. G. R. determined the N-DCX·Fab structure and helped in writing the manuscript. A. C. R. designed, performed, and analyzed the AUC studies. A. S. and M. O. S. designed, performed, and analyzed microtubule binding experiments. All authors contributed to preparing figures and/or writing of the manuscript.

Acknowledgments—We thank Joachim Diez and Santina Russo (Expose AG, Villigen, Switzerland) for data collection, the MX team at the Paul Scherrer Institut for the use of Swiss Light Source beam line X10SA, and Eric Kusznir (F. Hoffmann-La Roche Ltd.) for help with AUC data collection.

References

1. des Portes, V., Francis, F., Pinard, J. M., Desguerre, I., Moutard, M. L., Snoeck, I., Meiners, L. C., Capron, F., Cusmai, R., Ricci, S., Motte, J., Echenne, B., Ponsot, G., Dulac, O., Chelly, J., and Beldjord, C. (1998) doublecortin is the major gene causing X-linked subcortical laminar heterotopia (SCLH). *Hum. Mol. Genet.* **7,** 1063–1070
2. Deuel, T. A., Liu, J. S., Corbo, J. C., Yoo, S. Y., Rorke-Adams, L. B., and Walsh, C. A. (2006) Genetic interactions between doublecortin and doublecortin-like kinase in neuronal migration and axon outgrowth. *Neuron* **49,** 41–53
3. Knoth, R., Singec, I., Ditter, M., Pantazis, G., Capetian, P., Meyer, R. P., Horvat, V., Volk, B., and Kempermann, G. (2010) Murine features of neurogenesis in the human hippocampus across the lifespan from 0 to 100 years. *PLoS One* **5,** e8809
4. Kremer, T., Jagasia, R., Herrmann, A., Matile, H., Borroni, E., Francis, F., Kuhn, H. G., and Czech, C. (2013) Analysis of adult neurogenesis: evidence for a prominent "non-neurogenic" DCX-protein pool in rodent brain. *PLoS One* **8,** e59269
5. Taylor, K. R., Holzer, A. K., Bazan, J. F., Walsh, C. A., and Gleeson, J. G. (2000) Patient mutations in doublecortin define a repeated tubulin-binding domain. *J. Biol. Chem.* **275,** 34442–34450
6. Bahi-Buisson, N., Souville, I., Fourniol, F. J., Toussaint, A., Moores, C. A., Houdusse, A., Lemaitre, J. Y., Poirier, K., Khalaf-Nazzal, R., Hully, M., Leger, P. L., Elie, C., Boddaert, N., Beldjord, C., Chelly, *et al.* (2013) New insights into genotype-phenotype correlations for the doublecortin-related lissencephaly spectrum. *Brain* **136,** 223–244
7. Kim, M. H., Cierpicki, T., Derewenda, U., Krowarsch, D., Feng, Y., Devedjiev, Y., Dauter, Z., Walsh, C. A., Otlewski, J., Bushweller, J. H., and Derewenda, Z. S. (2003) The DCX-domain tandems of doublecortin and doublecortin-like kinase. *Nat. Struct. Biol.* **10,** 324–333
8. Fourniol, F. J., Sindelar, C. V., Amigues, B., Clare, D. K., Thomas, G., Perderiset, M., Francis, F., Houdusse, A., and Moores, C. A. (2010) Template-free 13-protofilament microtubule-MAP assembly visualized at 8 Å resolution. *J. Cell Biol.* **191,** 463–470
9. Moores, C. A., Perderiset, M., Francis, F., Chelly, J., Houdusse, A., and Milligan, R. A. (2004) Mechanism of microtubule stabilization by doublecortin. *Mol. Cell* **14,** 833–839
10. Liu, J. S., Schubert, C. R., Fu, X., Fourniol, F. J., Jaiswal, J. K., Houdusse, A., Stultz, C. M., Moores, C. A., and Walsh, C. A. (2012) Molecular basis for specific regulation of neuronal kinesin-3 motors by doublecortin family proteins. *Mol. Cell* **47,** 707–721
11. Bechstedt, S., and Brouhard, G. J. (2012) Doublecortin recognizes the 13-protofilament microtubule cooperatively and tracks microtubule ends. *Dev. Cell* **23,** 181–192
12. Bechstedt, S., Lu, K., and Brouhard, G. J. (2014) Doublecortin recognizes the longitudinal curvature of the microtubule end and lattice. *Curr. Biol.* **24,** 2366–2375
13. Cierpicki, T., Kim, M. H., Cooper, D. R., Derewenda, U., Bushweller, J. H., and Derewenda, Z. S. (2006) The DC-module of doublecortin: dynamics, domain boundaries, and functional implications. *Proteins* **64,** 874–882
14. Ericsson, U. B., Hallberg, B. M., Detitta, G. T., Dekker, N., and Nordlund, P. (2006) Thermofluor-based high-throughput stability optimization of proteins for structural studies. *Anal. Biochem.* **357,** 289–298
15. Pantoliano, M. W., Petrella, E. C., Kwasnoski, J. D., Lobanov, V. S., Myslik, J., Graf, E., Carver, T., Asel, E., Springer, B. A., Lane, P., and Salemme, F. R. (2001) High-density miniaturized thermal shift assays as a general strategy for drug discovery. *J. Biomol. Screen.* **6,** 429–440
16. Hausammann, G. J., Heitkamp, T., Matile, H., Gsell, B., Thoma, R., Schmid, G., Frasson, D., Sievers, M., Hennig, M., and Grütter, M. G. (2013) Generation of an antibody toolbox to characterize hERG. *Biochem. Biophys. Res. Commun.* **431,** 70–75
17. Kovari, L. C., Momany, C., and Rossmann, M. G. (1995) The use of antibody fragments for crystallization and structure determinations. *Structure* **3,** 1291–1293
18. Banner, D. W., Gsell, B., Benz, J., Bertschinger, J., Burger, D., Brack, S., Cuppuleri, S., Debulpaep, M., Gast, A., Grabulovski, D., Hennig, M., Hilpert, H., Huber, W., Kuglstatter, A., Kusznir, E., Laeremans, T., Matile, H., Miscenic, C., Rufer, A. C., Schlatter, D., Steyaert, J., Stihle, M., Thoma, R., Weber, M., and Ruf, A. (2013) Mapping the conformational space accessible to BACE2 using surface mutants and cocrystals with Fab fragments, Fynomers and Xaperones. *Acta Crystallogr. D Biol. Crystallogr.* **69,** 1124–1137
19. Hamers-Casterman, C., Atarhouch, T., Muyldermans, S., Robinson, G., Hamers, C., Songa, E. B., Bendahman, N., and Hamers, R. (1993) Naturally occurring antibodies devoid of light chains. *Nature* **363,** 446–448
20. Tereshko, V., Uysal, S., Koide, A., Margalef, K., Koide, S., and Kossiakoff, A. A. (2008) Toward chaperone-assisted crystallography: protein engineering enhancement of crystal packing and x-ray phasing capabilities of a camelid single-domain antibody (VHH) scaffold. *Protein Sci.* **17,** 1175–1187
21. Steyaert, J., and Kobilka, B. K. (2011) Nanobody stabilization of G protein-coupled receptor conformational states. *Curr. Opin. Struct. Biol.* **21,** 567–572
22. Pardon, E., Laeremans, T., Triest, S., Rasmussen, S. G. F., Wohlkönig, A., Ruf, A., Muyldermans, S., Hol, W. G. J., Kobilka, B. K., and Steyaert, J. (2014) A general protocol for the generation of Nanobodies for structural biology. *Nat. Protoc.* **9,** 674–693
23. Campbell, J. N., and Slep, K. C. (2011) $\alpha\beta$-Tubulin and microtubule-binding assays. *Methods Mol. Biol.* **777,** 87–97

24. Schuck, P. (2000) Size distribution analysis of macromolecules by sedimentation velocity ultracentrifugation and Lamm equation modeling. *Biophys. J.* **78,** 1606–1619
25. Brautigam, C. A. (2015) Calculations and publication-quality illustrations for analytical ultracentrifugation data. *Methods Enzymol.* **562,** 109–133
26. Delaglio, F., Grzesiek, S., Vuister, G. W., Zhu, G., Pfeifer, J., and Bax, A. (1995) NMRPipe: a multidimensional spectral processing system based on UNIX pipes. *J. Biomol. NMR* **6,** 277–293
27. Johnson, B. A., and Blevins, R. A. (1994) NMR View: a computer program for the visualization and analysis of NMR data. *J. Biomol. NMR* **4,** 603–614
28. Kabsch, W. (2010) XDS. *Acta Crystallogr. D Biol. Crystallogr.* **66,** 125–132
29. McCoy, A. J., Grosse-Kunstleve, R. W., Adams, P. D., Winn, M. D., Storoni, L. C., and Read, R. J. (2007) Phaser crystallographic software. *J. Appl. Crystallogr.* **40,** 658–674
30. Emsley, P., and Cowtan, K. (2004) Coot: model-building tools for molecular graphics. *Acta Crystallogr. D Biol. Crystallogr.* **60,** 2126–2132
31. Langer, G., Cohen, S. X., Lamzin, V. S., and Perrakis, A. (2008) Automated macromolecular model building for x-ray crystallography using ARP/wARP version 7. *Nat. Protoc.* **3,** 1171–1179
32. Smart, O. S., Womack, T. O., Flensburg, C., Keller, P., Paciorek, W., Sharff, A., Vonrhein, C., and Bricogne, G. (2012) Exploiting structure similarity in refinement: automated NCS and target-structure restraints in BUSTER. *Acta Crystallogr. D Biol. Crystallogr.* **68,** 368–380
33. Murshudov, G. N., Skubák, P., Lebedev, A. A., Pannu, N. S., Steiner, R. A., Nicholls, R. A., Winn, M. D., Long, F., and Vagin, A. A. (2011) REFMAC5 for the refinement of macromolecular crystal structures. *Acta Crystallogr. D Biol. Crystallogr.* **67,** 355–367
34. Adams, P. D., Afonine, P. V., Bunkóczi, G., Chen, V. B., Davis, I. W., Echols, N., Headd, J. J., Hung, L. W., Kapral, G. J., Grosse-Kunstleve, R. W., McCoy, A. J., Moriarty, N. W., Oeffner, R., Read, R. J., Richardson, D. C., *et al.* (2010) PHENIX: a comprehensive Python-based system for macromolecular structure solution. *Acta Crystallogr. D Biol. Crystallogr.* **66,** 213–221
35. Winn, M. D., Ballard, C. C., Cowtan, K. D., Dodson, E. J., Emsley, P., Evans, P. R., Keegan, R. M., Krissinel, E. B., Leslie, A. G., McCoy, A., McNicholas, S. J., Murshudov, G. N., Pannu, N. S., Potterton, E. A., Powell, H. R., *et al.* (2011) Overview of the CCP4 suite and current developments. *Acta Crystallogr. D Biol. Crystallogr.* **67,** 235–242
36. Letunic, I., Copley, R. R., Schmidt, S., Ciccarelli, F. D., Doerks, T., Schultz, J., Ponting, C. P., and Bork, P. (2004) SMART 4.0: towards genomic data integration. *Nucleic Acids Res.* **32,** D142–D144
37. Wishart, D. S., and Sykes, B. D. (1994) The ^{13}C chemical-shift index: a simple method for the identification of protein secondary structure using ^{13}C chemical-shift data. *J. Biomol. NMR* **4,** 171–180
38. Nooren, I. M., and Thornton, J. M. (2003) Diversity of protein-protein interactions. *EMBO J.* **22,** 3486–3492
39. Diederichs, K., and Karplus, P. A. (1997) Improved R-factors for diffraction data analysis in macromolecular crystallography. *Nat. Struct. Biol.* **4,** 269–275
40. Karplus, P. A., and Diederichs, K. (2012) Linking crystallographic model and data quality. *Science* **336,** 1030–1033